Assessment of CO2 and NOx emissions in intercooled pulsed detonation turbofan engines

ASSESSMENT OF CO_2 AND NO_X EMISSIONS IN INTERCOOLED PULSED DETONATION TURBOFAN ENGINES

Carlos Xisto,* Olivier Petit and Tomas Grönstedt
Dep. of Mechanics and Maritime Sciences
Chalmers University of Technology
Gothenburg, Sweden
Email: carlos.xisto@chalmers.se

Anders Lundbladh
GKN Aerospace
Trollhättan, Sweden

ABSTRACT

In the present paper, the synergistic combination of intercooling with pulsed detonation combustion is analyzed concerning its contribution to NO_x and CO_2 emissions. CO_2 is directly proportional to fuel burn and can, therefore, be reduced by improving specific fuel consumption and reducing engine weight and nacelle drag. A model predicting NO_x generation per unit of fuel for pulsed detonation combustors, operating with jet-A fuel, is developed and integrated within Chalmers University's gas turbine simulation tool GESTPAN. The model is constructed using CFD data obtained for different combustor inlet pressure, temperature and equivalence ratio levels. The NO_x model supports the quantification of the trade-off between CO_2 and NO_x emissions in a 2050 geared turbofan architecture incorporating intercooling and pulsed detonation combustion and operating at pressures and temperatures of interest in gas turbine technology for aero-engine civil applications.

Nomenclature

β	Purge fraction
η_b	Combustion efficiency
$\eta_{p,i}$	Component i polytropic efficiency
η_{prop}	Propulsive efficiency
$\eta_{thermal}$	Thermal efficiency

* Address all correspondence to this author.

λ	Last blade height (mm)
ϕ	Equivalence ratio
π	Pressure ratio
ρ	Fluid density (kg/m^3)
f	Fuel air ratio during fill
f_D	Friction factor
h_0	Stagnation enthalpy (J)
L	Length of the PDC chamber (m)
M_{CJ}	Detonation Mach number
n	Pressure ratio split exponent
P	Total pressure (Pa)
p	Static pressure (Pa)
P_{b}	Plateau pressure (Pa)
P_{CJ}	Chapman Jouget pressure (Pa)
P_{VN}	von-Neumman peak pressure (Pa)
T	Stagnation temperature (K)
t	time (s)
T_b	Plateau temperature (K)

Acronyms

ATW	Advance tube and wing aircraft
BPR	Bypass ratio
CFD	Computational fluid dynamics
CMC	Ceramics matrix composites
FB	Fuel Burn
HPC	High-pressure compressor
IPC	Intermediate-pressure compressor
LTO	Landing and take-off
MTOW	Maximum take-off weight
OEW	Operational empty weight
OPR	Overall pressure ratio

PDC Pulsed detonation combustor

SFC Specific fuel consumption mg/N·s

T/O Take-off

TET Turbine entry temperature (K)

TOC Top-of-climb

Subscripts

f Fill state

p Purge state

s Scavage state

1-138 Station designation shown in Fig.7

4 PDC cycle averaged properties

comp. Compression system (not including PDC)

1 Introduction

In Europe's H2020 programme the ULTIMATE project [1] is developing concepts for the next generation of gas turbine aero-engines, expected to enter service in 2050. The primary goal of the project is to accomplish the challenging reductions in CO_2 and NO_x emissions set forth by the European Commission in Flightpath 2050, Europe's Vision for Aviation. The "ULTIMATE" engines rely on conventional gas turbine technology and synergistically exploring the combination of radical technologies to simultaneously attack the major loss sources occurring in state of the art turbofan engines [2]: i) combustor irreversibility, ii) excess of kinetic energy in the bypass duct; iii) heat contained in core exhaust gases. ULTIMATE, targets each one of these losses by integrating different radical technologies in conventional gas turbine architectures. Intercooling and recuperation allow for a significant reduction of core nozzle exhaust temperature, thus decreasing loss source iii). The process of heat addition during constant pressure used in the Joule-Brayton cycle will always generate an excess of entropy, being responsible for a substantial loss of work potential. One way of considerably reduce such a loss is to introduce some kind of pressure rise combustion system, e.g., pulsed detonation combustor. The combination of intercooling together with constant volume combustion allows for a direct attack on loss source i) and iii). Such a combination is also expected to result in a synergy, since intercooling reduces the combustor inlet temperature, improves combustor volumetric efficiency and allows for more air-fuel to be combusted per engine cycle, which in turn increases core specific power [3] and contributes to a further reduction of loss source iii). Reducing the combustor inlet temperature also allows for an increase in combustion pressure ratio, reducing the risk of pre-ignition and reduces the cooling requirements of the pulsed detonation core.

1.1 NO_x formation in pulsed detonation combustion

The improvement in thermal efficiency is heavily linked to an increase in turbine entry temperature (TET) and overall pressure ratio (OPR). However, thermal NO_x is primarily driven by the combustion temperature. Thus improving thermal efficiency will increase the combustion temperature, causing an increase in NO_x production. Unless a cycle is carefully selected, a thermodynamically fuel-efficient engine could, therefore, generate more NO_x. The same principle applies to pulsed detonation cores, and it is further aggravated by the temperature increase due to detonation, especially at the high fuel–air ratio necessary to ensure the mixture's detonability.

Yungster et al. [4, 5], investigated the mechanisms behind NO_x formation in pulsed detonation cores using hydrocarbon– and hydrogen–air mixtures. The tube length plays an important role since it directly affects the residence time. Due to non-stationary effects, the formation of NO_x in a PDC tube is different from the one found in a conventional burner. At a given detonation tube section, the pressure and temperature profiles are characterized by short periods (tens of microseconds) of peak pressure and temperature, resulting from the passage of the detonation wave that accelerates the flow locally to supersonic conditions. This period is then followed by an expansion period until a plateau state of constant high temperature and high pressure is reached. The plateau is finally disturbed by the arrival of a reflection wave that starts the exhaust period until an equilibrium pressure is achieved. The aforementioned periods can be used to derive different residence times [5].

Figure 1 illustrates the typical detonation residence times, as well as the instantaneous temperature field occurring in a single PDC tube during the active period of detonation. The residence time t_1 is defined as the time it takes for the detonation wave to reach the open end of the tube. A second characteristic time, t_2, is defined by the arrival of the expansion wave at the valve (close end of the tube). For this ideal representation, the temperature and pressure in the valve region are constant for the period $t < t_2$. After t_2 the blowdown process starts and the temperature inside the detonation tube drops. Both times are a function of the mixture properties, initial conditions and tube length. Therefore, for a given set of properties and initial conditions, reducing the tube length will allow for a reduction of residence time and associated formation of NO_x. Yungster and Breisacher [4] reported that for a stoichiometric jet-A–air mixture an increase from 0.5 m to 1 m in tube length resulted in a 30% increase in NO_x emissions.

The fuel-air ratio plays a significant role in emissions, and the formation of NO_x reaches its maximum value on the fuel-lean side of stoichiometric. Therefore, a way of decreasing the NO_x formation is to burn lean or rich mixtures. Detonating in fuel-lean mixtures reduces the amount of generated NO_x due to a reduction of peak temperature and pressure. In a gas turbine, the practical usage of lean mixtures improves engine performance and also reduces NO_x emissions indirectly by burning less fuel. However, achieving detonation in lean mixtures is extremely difficult. Burning fuel-rich mixtures reduce NO_x primarily due to the competition between fuel and nitrogen for oxygen, but it also requires a secondary combustion system to burn the excess fuel.

The effect of initial pressure and temperature on NO_x formation, in jet-A–air mixtures, was also analyzed in [4]. The results reported a 75% increase in NO_x when the initial temperature and pressure increased from 298 K and 1 bar to 700 K and 8 bar, respectively. Intercooling helps to reduce the combustor inlet temperature, which contributes to a reduction of detonation temperature and a possible

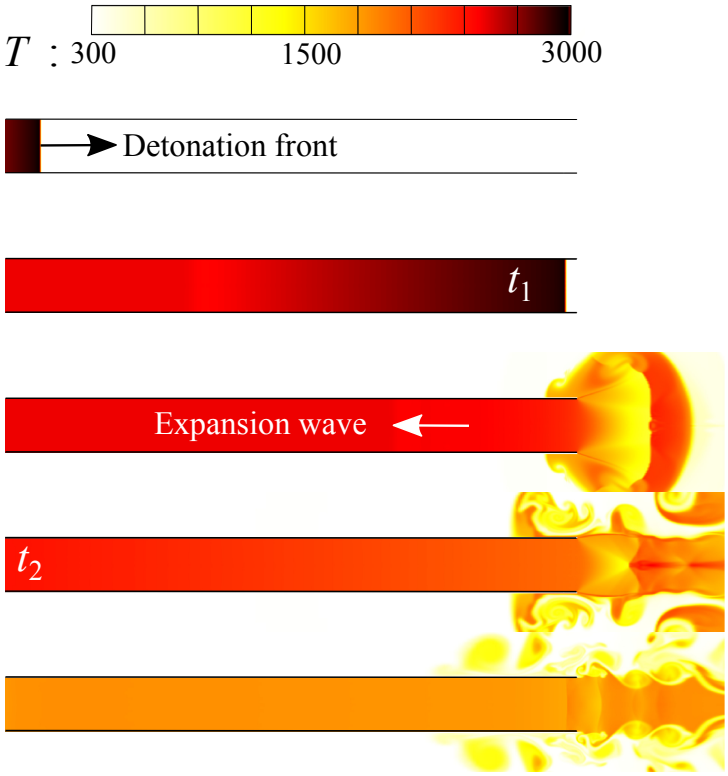

FIGURE 1. Detonation propagation and blowdown characteristic times occurring during the active detonation period.

reduction of NO_x formation. The usage of intercooling to reduce the combustor inlet temperature for a given inlet pressure is proposed as a possible solution to control NO_x formation in pulsed detonation cores.

NO_x formation in pulsed detonation combustion can also be controlled by employing more complex NO_x abatement techniques, such as re-circulation of exhaust gas, the injection of steam or the usage of stratified charges. The effect of exhaust gas re-circulation was investigated by Djordjevic et al. [6] in H2–air mixtures with promising results. The usage of stratified charges was explored by Yungster and Breisacher [4] for jet-A–air mixtures and revealed that filing different sections of the tube with different fuel-air ratios can contribute to a promising reduction of NO_x emissions.

In the present paper, an $EINO_x$ model is derived and integrated into a gas turbine performance code. The model was implemented using CFD data obtained for different combinations of combustor inlet pressure, temperature and equivalence ratio levels. The $EINO_x$ model supports the quantification of NO_x emissions in an optimized 2050 geared turbofan architecture incorporating intercooling and pulsed detonation combustion. To the best knowledge of the authors, this paper represents the first attempt to establish NO_x emissions while considering temperatures and pressures of interest for civil aero-engine applications of gas turbine technology.

2 EINO$_x$ model for Jet-A

In the present section, the model for EINO$_x$ is derived. The model gives predictions of thermal EINO$_x$ (g/kg fuel) for a given set of inflow conditions, such as equivalence ratio, ϕ, initial temperature, T_{33}, and pressure P_{33}, see Table 1. The predictions are obtained using CFD computations and used to generate tabulated data for a given ϕ. The tabulated data is then integrated into the engine performance code allowing for the EINO$_x$ estimation for any given combination (within the boundaries of Table 1) of PDC inflow temperature and pressure.

2.1 Numerical methodology

The numerical method used to derive the EINO$_x$ model is based on the finite volume implementation of the one-dimensional multi-species Euler equations using Ansys Fluent [7]. The finite-rate reactions are calculated with Arrhenius kinetic expressions and, due to the supersonic nature of the flame, a laminar finite-rate model is selected. A reduced chemical mechanism, comprising 46 reactions and 24 species [4], is used to model detonation (see Appendix).

The equations are time-discretized using the second-order backward implicit Euler method. For the inner iterations, a 3 stage Runge-Kutta method is employed. A constant time-step ranging from 10^{-9} s to 10^{-10} s is imposed to advance in time. To evaluate the convective fluxes, the Roe flux-difference splitting scheme is used together with a second-order upwind scheme for variable interpolation. The fluid is assumed to behave as a semi-perfect gas.

The present analysis does not account for the effect of detonation initiation or the effect of the transition from deflagration to detonation in EINO$_x$. Instead, an approach similar to the one used by [8], here illustrated in Fig. 2, is used. The tube is divided into two different regions. The first region is used for detonation initiation by patching a high pressure and high-temperature trigger gas close to the tube valve. The detonation wave is allowed to travel for a distance of 20 cm until a fully developed detonation profile is achieved. This distance was found sufficient for the establishment of a self-sustained detonation wave in the present simulations. The subsequently established detonation wave then travels to the detonation tube where EINO$_x$ is computed.

The usage of a 1D model neglects the cellular pattern of the detonation front that consists in pockets of high pressure and temperature. Neglecting the three-dimensional cellular structure of a detonation front might result in an under-prediction of EINO$_x$. However, computing such pattern is extremely demanding in terms of CPU power and time. Still, assuming a one-dimensional planar detonation front has been applied with success in previous works [5, 8] and is here employed, as it gives a good compromise between accuracy and computational effort.

TABLE 1. Parameter variation used in the derivation of the EINO$_x$ model.

ϕ	0.6–1.0					
P_{33} (bar)	1.0	8.6	20	30	50	60
T_{33} (K)	200–880					

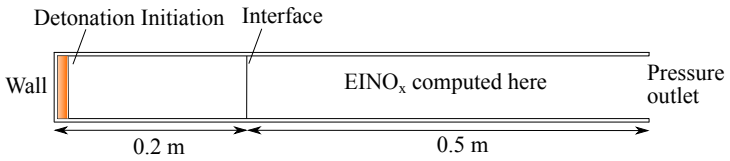

FIGURE 2. 1D-model used to EINO$_x$ evaluation.

Regarding boundary conditions, in the left side of the tube, a slip wall boundary condition is imposed to represent the valve plane. In right side of the tube (open side) a pressure outlet condition is specified, imposing a fixed static pressure (equal to P_{33}) if the flow is subsonic, and extrapolating the pressure from the domain interior if the flow is supersonic. EINO$_x$ variations across the outlet are accounted for and the cumulative value is added to the remaining EINO$_x$ computed inside the tube.

2.2 Grid refinement study

A grid sensitivity study was performed to evaluate the impact of grid resolution on results. Four 1-D grids with increased resolution are analyzed: grid-A, $\Delta x = 0.5$ mm; grid-B, $\Delta x = 0.25$ mm; grid-C, $\Delta x = 0.125$ mm; and grid-D, $\Delta x = 0.0625$ mm. The results obtained for the pressure distribution at a given time instance together with the theoretical Chapman Jouguet pressure, P_{CJ}, are plotted in Fig. 3. The data is computed in a tube with length equal to 0.5 mm, for inflow temperature and pressure of 700 K and 8.6 bar, respectively. It is noted that the results are obtained at the same time instance but intentionally translated along the x-axis (showed for grid-D in Fig. 3) for a better comparison. The predicted detonation velocity is very similar across the grids. The predicted von-Neumann peak pressure increases with grid resolution, however the impact of exactly resolve the peak pressure is not expected to influence the NO$_x$ generation since it occurs in a very small time interval. The agreement between the theoretical and predicted value of Chapman Jouguet pressure is good and consistent in all grid resolutions. The aforementioned behavior is reflected in plateau pressure, P_b, that is almost identical across all grids.

Figure 4 shows that the relative difference between the EINO$_x$ computed with grid-C and grid-D is below 1%. Therefore, grid-C should be selected for constructing the EINO$_x$ model since it gives a good compromise between accuracy and computational time.

2.3 Validation

Figure 5 shows a comparison between the CFD computed EINO$_x$ and literature data [4]. The results are obtained for a tube with 0.5 m length and inflow temperature and pressure of 700 K and 8.6 bar, respectively. The results show a good agreement for EINO$_x$ at different equivalence ratios. The differences are probably related to different detonation initiation assumptions used by Yungster and Breisacher since they have included the effect of detonation initiation in their calculations. It is noted that the literature data used for validation [4] was obtained with a numerical model but was validated with experimental results.

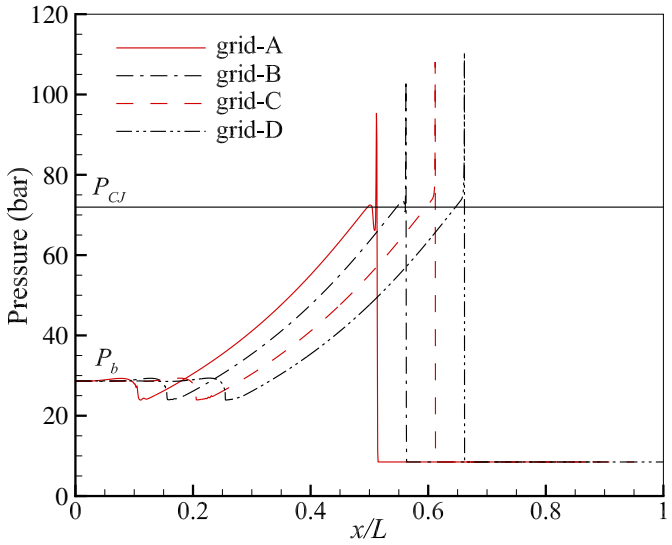

FIGURE 3. Pressure distribution in the tube using different grid resolutions. Note: the curves are intentionally translated along the x-axis (showed for grid-D) allowing for a better comparison.

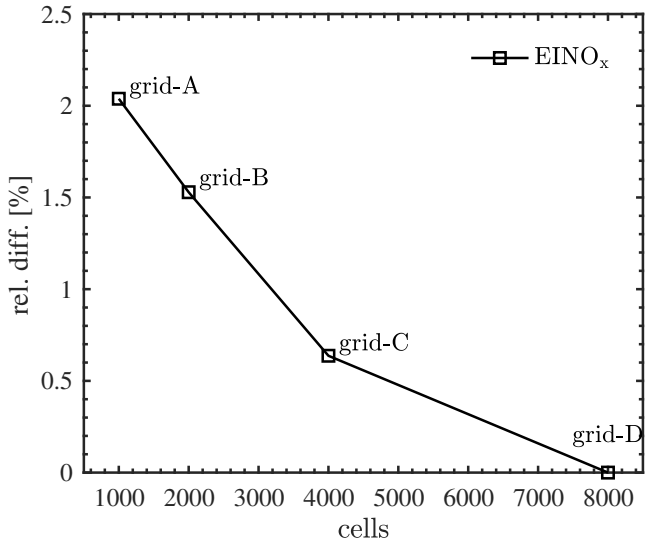

FIGURE 4. Relative difference computed for the EINO$_x$

3 Engine performance modeling

This section describes the methodology employed to model the different engines and estimate mission fuel burn. It starts by presenting the optimized reference 2050 turbofan engine and crucial associated component data. Afterwards, the intercooled pulsed detonation turbofan engine is detailed together with its most essential components and respective modeling assumptions. The section

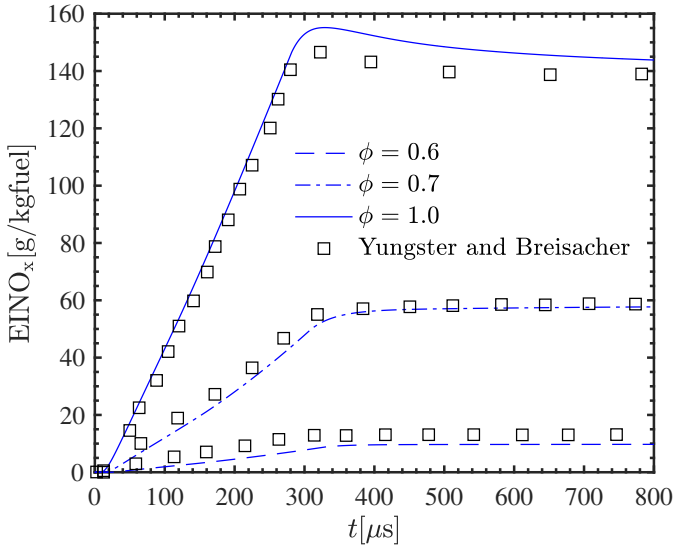

FIGURE 5. Validation against literature [4] data, P_{33} = 8.6 bar, T_{33} = 700 K, L = 0.5 m

ends with the description of the engine weight and aircraft models.

Chalmers University's in-house simulation tool called GESTPAN (GEneral Stationary and Transient Propulsion ANalsysis) [9] is used to predict the aero-engines performance. GESTPAN is a generalized simulation system for the prediction of gas turbine performance in design, off-design and transient conditions. GESTPAN has been extensively used and validated across several gas turbine aero-engine applications [2, 10–14].

3.1 Reference engine

An ultra-high bypass ratio geared turbofan is defined as year 2050 reference engine for a long-range twin-engine aircraft applications. The technological assumptions include the usage of ceramics matrix composite high-pressure turbine stator vanes, with improved thermal capabilities. The engine model assumes a reduction of secondary air system flows by improving annulus sealing and improvements in turbomachinery efficiencies are constrained by sizing effects in high-pressure turbomachinery. Cycle temperatures and OPR are specified to comply with material temperature limitations and to minimize NO_x and particle emissions. Advanced lightweight materials and improved manufacturing techniques are assumed for the weight and structural considerations [15, 16]. The cruise point component efficiencies and cycle temperature limits are listed in Table 2. The aforementioned technological assumptions are based on historical trends and the consensus of ULTIMATE consortium industry partners.

The engine schematic is given in Fig. 6 (bottom half), and the respective station numbering are given in Fig. 7. It is noted that the blue/dashed modules represent the intercooled engine and that the PDC module is replaced by a burner module in the reference configuration. The reference engine features a geared fan and a three-stage high-speed booster, both driven by a four-stage high-speed

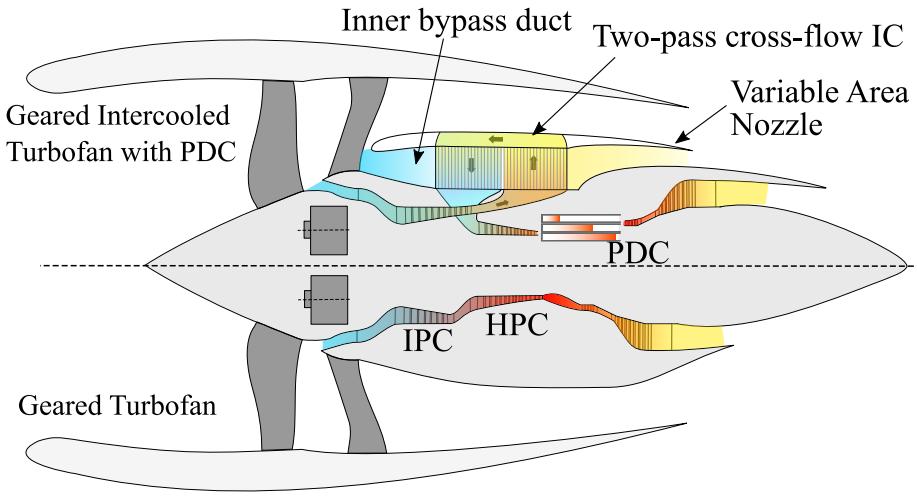

FIGURE 6. Top: the geared intercooled gas turbine engine with PDC. Bottom: reference geared turbofan engine.

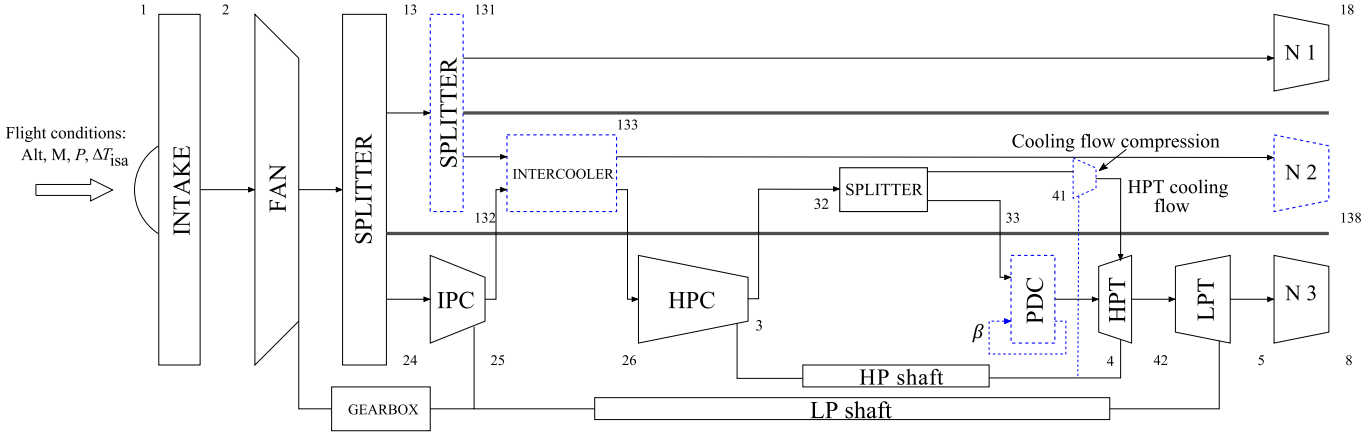

FIGURE 7. Performance model schematics for the reference and intercooled engines.

low-pressure turbine. The high-pressure system comprises an all-axial ten-stage compressor driven by a two-stage turbine.

3.2 Geared turbofan intercooled PDC engine model

The geared intercooled PDC turbofan engine is illustrated in Fig. 6 (top-half) and the respective station numbering (blue/dashed modules) are given in Fig. 7. The engine now includes a pulsed detonation combustor and a heat-exchanger (HEX) located in a secondary inner bypass duct.

3.2.1 Intercooler The intercooler model represents a two-pass cross flow tubular HEX developed by [13,17,18]. The geometry was optimized to maximize aerodynamic efficiency and heat transfer rate. The HEX is located between the IPC and HPC and is used

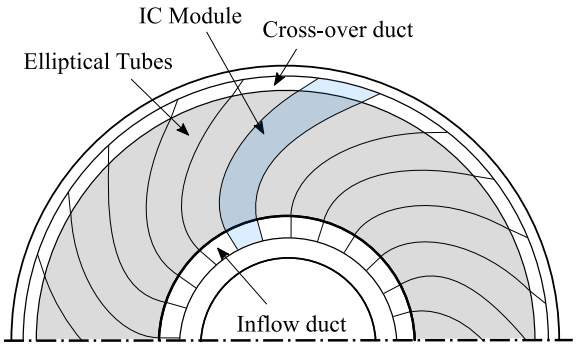

FIGURE 8. Schematic of the intercooler arrangement around the annulus.

to cool the IPC delivery air. The core flow is first diffused in the inflow duct before entering the first stack of tubes. The two stacks are connected with a cross-over duct. The flow then enters the second tubular heat exchanger and is finally accelerated in the outflow duct to match the required HPC inflow conditions. The external side of the intercooler comprises a diffuser duct that reduces Mach number at the IC external side, increasing heat transfer and reducing pressure losses. The spent cooling air is ejected through a variable area nozzle N2 and is recovered as thrust. The variable area nozzle allows for a greater control of the amount of rejected heat as well as a reduction of the intercooler external Mach number and its associated pressure losses. Being able to control the amount of transferred heat throughout a mission introduces one additional degree of freedom in the optimization loop. The intercooler comprises 24 separated modules distributed around the annulus in an involute spiral way, ensuring the most optimum utilization of available space, see Fig. 8.

Pressure loss and heat transfer correlations were derived using CFD in [17] for each one of the intercooler sub-components (ducts,

TABLE 2. Cruise point component efficiencies and cycle temperature limits.

Parameter	Value
$\eta_{p,\text{FAN}}$	0.95
$\eta_{p,\text{IPC}}$	0.93
$\eta_{p,0,\text{HPC}}$	0.89
$\eta_{p,\text{HPT}}$	0.89
$\eta_{p,\text{LPT}}$	0.94
η_b	0.9995
TET (T/O)	< 1920 K
TET (TOC)	< 1890 K
TET (cruise)	< 1540 K
T_3 (cruise)	< 880 K
T_3 (T/O) (cases with PDC)	< 880 K

tubes, connections). The correlations are detailed in [13, 17, 18], and the most important ones are repeated here for convenience. For the inflow duct, the pressure loss correlation is valid in the Re number range of 500,000 to 1,400,000:

$$K_{inflow} = \frac{p_{out} - p_{in}}{P_{in} - p_{in}} = -1.626 \times 10^{9} \mathrm{Re}^{-1.837} + 0.5513 \tag{1}$$

Regarding the cross-over duct, the pressure loss correlation is valid in the Re number range of 100,000 to 350,000:

$$K_{cr} = \frac{p_{in} - p_{out}}{P_{in} - p_{in}} = 3.128 \times 10^{-7} \mathrm{Re} + 10.1 \tag{2}$$

Finally, the pressure loss correlation, K, in the outflow duct is valid in the Re number range of 1,500,000 to 5,500,00:

$$K_{out\,flow} = \frac{P_{out} - P_{in}}{P_{out} - p_{out}} = 1.9 \times 10^{11} \mathrm{Re}^{-2.1} + 0.081 \tag{3}$$

In the equations above, the subscripts *out* and *in* refer to the individual duct inlet and outlet conditions. The summation of the individual pressure losses across the internal sub-components and connections of the intercooler allows for the derivation of the overall internal side (engine core side) pressure loss. The external side pressure loss is obtained through reference [19]:

$$\Delta P = \frac{(g_{1,in}/A_c)^2}{2\rho_{in}} \left[f_D \frac{A_w}{A_c} \frac{\rho_{in}}{\rho_m} \left(1 + \xi^2\right) \left(\frac{\rho_{in}}{\rho_{out}} - 1 \right) \right] \tag{4}$$

where $g_{1,in}$ is the intercooler external side mass flow rate, A_c is the minimum flow cross section area, A_w is the heat transfer wall area, ρ_{in} and ρ_{out} are the fluid density at the inlet and outlet, respectively, whereas ρ_m is the average between ρ_{in} and ρ_{out}. The parameter ξ is the ratio between the minimum flow cross-section area to the intercooler frontal area. The friction factor, f_D, is represented by a Re number correlation, valid in the range of $10,000 < \mathrm{Re} < 110,000$:

$$f_D = 0.01044 e^{-6.806 \times 10^{-5} \mathrm{Re}} + 0.008109 e^{-2.908 \times 10^{-6} \mathrm{Re}} \tag{5}$$

The heat transfer coefficient on the external side is defined using the Colburn factor:

$$j = \mathrm{St} \cdot \mathrm{Pr}^{2/3} = \frac{\mathrm{Nu}}{\mathrm{Re} \cdot \mathrm{Pr}} \mathrm{Pr}^{2/3} \tag{6}$$

where St is the Stanton number, Pr is the Prandtl number and Nu is the Nusselt number. A correlation for Colburn factor was derived using CFD and is valid in the range of $10,000 < \mathrm{Re} < 110,000$:

$$j = 0.003469 e^{-7.117 \times 10^{-5} \mathrm{Re}} + 0.003461 e^{-3.793 \times 10^{-6} \mathrm{Re}} \tag{7}$$

The location of the intercooler in the compression system is a trade-off between thermal efficiency and installation effects. Placing the intercooler earlier in the compression system benefits the engine thermal efficiency but also increases the intercooler volume and weight [20]. On the other hand, moving the intercooler further into the compression system allows for a reduction in volume, weight and pressure losses. This effect is fully accounted for in the present intercooler modeling approach. The pressure ratio split exponent [13],

$$n = \log_{\pi_{comp}} \left(\frac{P_{25}}{P_2} \right) \tag{8}$$

is therefore introduced. In Eq. (8) π_{comp} accounts for the pressure ratio in the compression system only. According to Zhao et al. [13], for a gear turbofan application, an optimum value for n is approximately 0.4. The effect of the pressure rise combustion system in the pressure ratio split exponent is further explored in the present paper.

3.2.2 Pulsed detonation combustor The PDC model is described in detail in [3], and some of the most important equations are here repeated for convenience. The model relies on chemical equilibrium relations and gas dynamic theory to predict mass-averaged PDC outlet properties, such as pressure rise,

$$\pi_{PDC} = \frac{P_b}{P_3} \cdot \left(\frac{\rho_f - \rho_s}{\rho_f + \rho_p} \right) + \frac{P_3}{P_3} \cdot \left(\frac{\rho_p + \rho_s}{\rho_f + \rho_p} \right) \tag{9}$$

where ρ_f, ρ_p and ρ_s are fill, purge and scavage densities, respectively. The outlet temperature, T_4, is obtained by iterating on the energy flows using the energy conservation equation,

$$q = (1 + f_4) \cdot \Delta h_{0,4-298K}(T_4, f_4) - \Delta h_{0,1-298K}(T_3) \tag{10}$$

where the overall fuel-to-air mass ratio is balanced by the purge fraction, β, and combustion efficiency, η_b

$$f_4 = f \cdot \frac{1-\beta}{\eta_b} \tag{11}$$

and the overall heat addition is $q = f_4 \cdot LHV$. The model will iterate on T_4 until q_4 is satisfied. The cycle-averaged fuel mass flow rate is given by:

$$\dot{m}_{fuel,4} = f_4 \cdot g_3 \tag{12}$$

The design cycle average temperatures are limited to the reference engine cycle TET by iterating on purge fraction,

$$\beta = \frac{\rho_p}{\rho_f + \rho_p} \tag{13}$$

On the other hand, no limitation is imposed on the combustor exit pressure and the reference engine combustion efficiency is assumed. Purge fraction is also used to iterate on PDC outlet parameters in off-design conditions. The PDC includes a high-frequency intake valve, modelled as a sudden expansion with a complete loss of dynamic pressure. The fill and purge Mach number is fixed at $M_f = 0.2$, therefore a complete loss of dynamic pressure results in a 3% loss in total pressure across the valve. The filling equivalence ratio controls the maximum pressure and temperature occurring during the PDC cycle. Fuel–air mixtures close to stoichiometric conditions will result in higher Chapman-Jouguet pressure and temperature and will ultimately act as a constraint for weight and NO_x emissions. Different levels of fuel-air ratio will be analyzed in the present paper.

One additional constraint is introduced for the pulsed detonation combustor test cases in order to account for the effects of auto-ignition delay time in high pressure, high-temperature jet-A–air mixtures. The auto-ignition delay time for jet-A–air mixtures is in the

order of 2.0–4.0 ms for a mixture temperature of 833 K and pressure around 30 bar at equivalence ratios ranging from 0.7–1.0 [21]. Therefore the temperature at take-off conditions is limited to 880 K for the optimized pulsed detonation cores.

3.2.3 High-pressure turbine The high-pressure turbine located downstream of the PDC is exposed to rapid periodic changes in operating conditions. The time-dependent thermodynamic properties will subject the turbine to substantial variations in mass flow and rotor flow incidence angles [22] and might lead to periods of flow separation, negative torque and reverse flow [23]. In the early stages of detonation (Det.), see Fig. 9, the turbine is also subjected to non-stationary shock waves [24, 25] that possibly contribute to additional boundary layer losses. These mechanisms have a negative impact on the turbomachinery efficiency and can negate the theoretical improvements of detonation in cycle efficiency. Other effects like tube-to-tube interference in sequential detonation combustion are also important and unique to pulsed detonation flows. In the present analysis, the high-pressure turbine design efficiency is reduced from 90.2% to 85% in order to account for the losses arising from the interaction with PDC flow, based on the findings reported in [26] and on in-house PDC-coupled turbine simulations. No penalty is considered on the efficiency of the compressors and low-pressure turbine.

3.2.4 Cooling requirements The static components in the two-stage HP turbine are fabricated from ceramic matrix composites (CMC) and will not include film cooling. The rotor blades are fabricated from advance nickel alloys with a melting point limit of 1400K. The entire HPT is cooled with HP compressor bleed air. However, due to the incorporation of a pressure rise combustion system, the bleed cooling air is at a lower pressure and requires further compression in order to match the PDC outlet pressure and to provide a pressure margin to enter the core through the vane and rotor cooling passages.

A radial compressor is placed between the splitter and HPT, and the power necessary to drive the radial compressor is extracted from the high-pressure shaft. The effect of intermittent PDC flow is expected to disturb the boundary layer and affect the performance of film cooling. However, the full extension of such phenomena is not fully comprehended at this stage and therefore not accounted for in the present analysis.

The cooling air requirement for the rotor blades and discs is reduced from current state-of-the-art technology, by assuming improved sealing and the usage of cooled cooling air during take-off and climb. For the reference engine, the cooling air percentage is fixed to 6.3% throughout the entire flight envelope. The geared intercooled pulsed detonation core is constrained by the same temperature limits. Therefore it will be expected that both engines employ similar levels of cooling. Intercooling allows for a reduction of HPC delivery temperature. However, the secondary cooling compression system required by the pulsed detonation core will increase the cooling flow temperature back to that of the reference engine level.

3.2.5 Scale effects Intercooling and pressure-rise combustion have the potential to deliver significant improvements in thermal efficiency. Both technologies also contribute to an increase in core specific power, which will contribute to lower core mass flow and increases in BPR. Moreover, aircraft aerodynamic efficiency improvements, reductions in structural weight and fuel payload an-

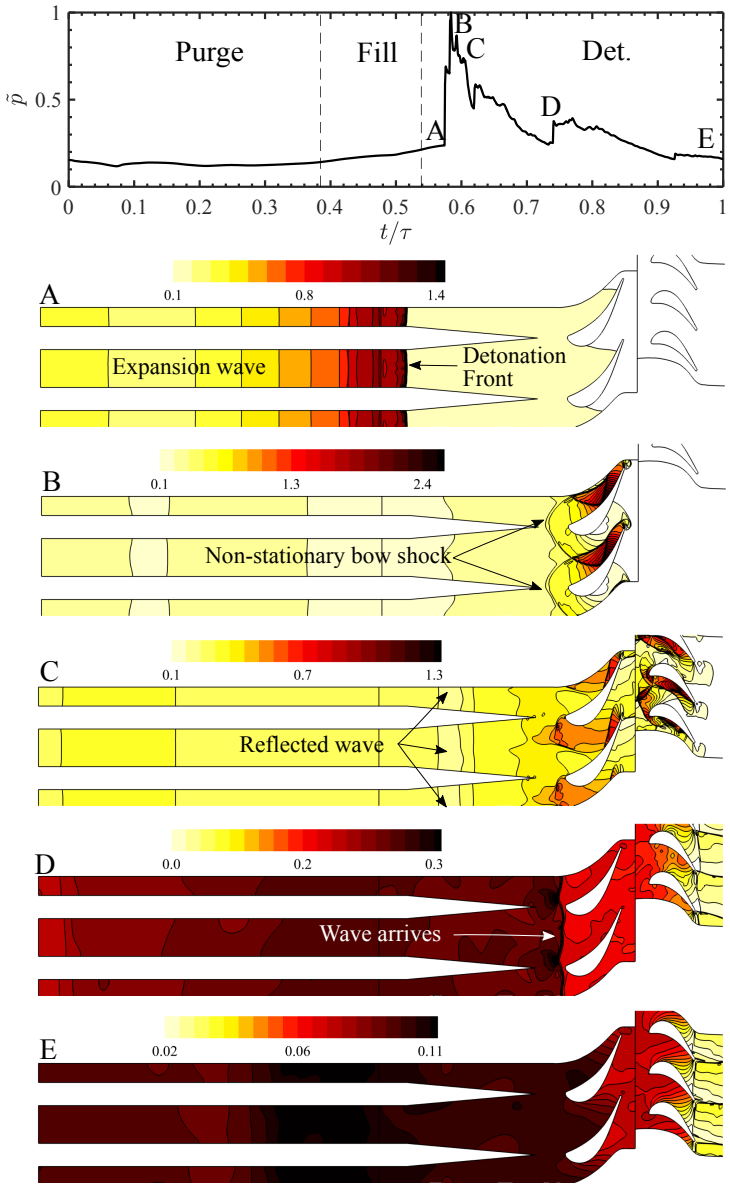

FIGURE 9. In-house CFD results obtained for the mass-weighted averaged normalized static pressure history, computed at turbine inlet. Instantaneous contour plots of static pressure illustrating the complex shock-wave structure occurring in the rotor and stator planes.

ticipated in 2050 will reduce thrust requirements. These effects combined will result in the introduction of smaller and less efficient turbomachinery components. In the present analysis, the polytropic efficiency of the HPC is corrected to reflect changes in last stage blade height [27],

$$\eta_{p,\mathrm{HPC}} = \eta_{p,0,\mathrm{HPC}} + \left(0.0532 - \frac{0.5547}{\lambda} - \frac{1.7724}{\lambda^2}\right) \tag{14}$$

where λ is the last blade height in mm. For calculating the last blade height it is assumed an HPC exit hub-to-tip ratio of 0.92 and axial Mach number of 0.27. The correlation given in Eq. (14) is used for every HPC designs generated in the optimization loop. However in reality it would need to be corrected for different operating conditions, stage-count, etc.

3.3 Engine weight model

Engine weight is assessed using Chalmers in-house WEICO (WEIght and COst estimation) tool. WEICO is implemented using the same principles of [28], and its validation was supported by EU FP6 VITAL [29] and NEWAC [30] projects. WEICO allows for an estimation of component-based weight for the conventional turbomachinery. In order to support conceptual design, WEICO can also be used to generate cross-sectional drawings for conventional gas turbine technology. Details about the usage and methodology of WEICO are given in Refs. [31, 32]. Additional weight models were developed for the intercooler and pulsed detonation core. The intercooler is fabricated from titanium, and its weight is calculated based on the estimation of the required number of tubes and ducts, internal and external pressures, and material properties. Details on the assumptions can be found in [33].

The weight of the PDC is estimated assuming that each duct is 1 m long and has a cross-sectional area equal to 50 mm × 50 mm. The material is a Nickel-based alloy with density equal to 8300 $\mathrm{kg/m^3}$, tensile strength equal to 83 ksi (aprox. 572 MPa). The thickness of each duct is dimensioned at take-off conditions using the von-Neumann pressure spike,

$$\delta = \frac{P_{VN,\mathrm{T/O}} \cdot 1.5 \cdot D_{duct}}{2 \cdot \sigma} \tag{15}$$

which is the highest pressure occurring in the ducts during the propagation of the detonation wave, for which a safety factor of 1.5 is employed. It is also assumed that the total cross-sectional area of the ducts is two times the required steady-state equivalent cross-sectional area, for a given inlet Mach number of 0.2. This means that during operation half of the ducts will be detonating while the other half will be filling/purging. The total weight of the detonation ducts is given by the product of the duct metal volume by the material density and number of ducts. The detonation ducts are surrounded by a shell, and the gap between the shell and the ducts is equal to 20% of the duct height, which should be sufficient to accommodate the combustor cooling flow. The thickness of the shell is computed using the HPC delivery pressure at take-off conditions, and the weight of the shell is derived by multiplying the volume of metal with the material density. The accessories weight is assumed to be 30% of the sum of shell and detonation ducts weight.

3.4 Aircraft model

The aircraft model used in the present work has been reported in [34], where two aircraft concepts were developed for intra-European and intercontinental missions, respectively. The concepts are based in advance tube and wing (ATW) aircraft designs for year 2050 entry

into service. The intercontinental twin engine 300 passenger aircraft with a maximum payload range of 11,800 km is selected for the present work. Improvements in aerodynamic efficiency are achieved by incorporating different technologies that minimize drag and/or induced drag, (e.g., high aspect ratio wings, laminar flow nacelles, hybrid laminar flow control in wing and tail). This allows achieving a maximum lift over drag of approximately 24.6 at mid cruise conditions. The operational empty weight is reduced with an increased utilization of carbon fiber reinforced polymers, by incorporating improved cabin furnishing and accessories and through the usage of a fly-by-light system. A maximum take-off weight (MTOW) of 187,900 kg is obtained for the ATW incorporating the reference gear turbofan engine. For the intercooled pulsed detonation engine, the MTOW will change in every optimization iteration to account for the engine installation and performance.

The model is built around the usage of interpolation tables that allow for the derivation of different aircraft performance metrics (drag, Operational Empty Weight (OEW), MTOW, nacelle drag, thrust requirements, etc.) for a given combination of engine performance (SFC) and installation effects (engine weight, and fan diameter). Therefore each point in the table represents a re-scaled aircraft. Mission-related SFC is estimated using the different flight phases,

$$\mathrm{SFC} = a \cdot \mathrm{SFC}_{\mathrm{cruise}} + b \cdot \mathrm{SFC}_{\mathrm{TOC}} + c \cdot \mathrm{SFC}_{\mathrm{T/O}} \tag{16}$$

In Eq. (16) a, b, and c are weighting factors based on the fuel consumption in each of the flight phases represented in Table 3. Engine weight and fan diameter are estimated using WEICO.

3.5 Engine optimization

The engines optimization loop is illustrated in Fig. 10. The engines are optimized by varying design values of bypass ratio, BPR, fan pressure ratio, π_{FAN}, IPC pressure ratio, π_{IPC}, and HPC pressure ratio, π_{HPC}. The SFC results obtained from the engine performance tool (GESTPAN) are inserted into the aircraft performance model (ATW2050). The thermodynamic data generated by GESTPAN is read by the engine weight and dimensions model (WEICO). The engine weight and fan size is afterwards computed with WEICO and also inserted into the aircraft model. The aircraft model will finally compute fuel burn for a given mission. The aforementioned approach

TABLE 3. Mission points representing the different flight phases of the ATW 2050 aircraft.

Parameter	Mid-Cruise	Max Climb (TOC)	Max Takeoff (T/O)
ΔT_{ISA} (K)	0.0	10.0	15.0
Alt. (m)	11,277	10,668	0.0
Mach	0.8	0.82	0.2
Weight. f.	$a = 0.929$	$b = 0.061$	$c = 0.010$

allows for the engines to be optimized for minimum fuel burn for a fixed mission, accounting for the effects of engine weight, installation (fan and nacelle diameter) and engine performance (SFC). The optimization constraints and component efficiencies are listed in Table 2. The mathematical method used for optimization is the sequential quadratic programming (SQP) inspired in the work of [35] and is fully integrated into the engine optimization tool.

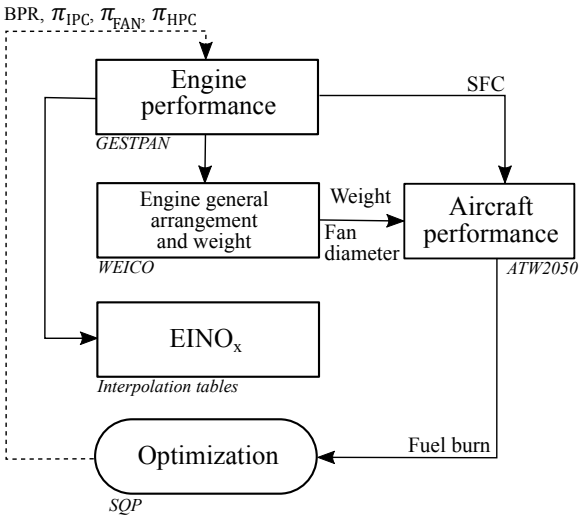

FIGURE 10. Engine optimization loop

4 Results

In this section, the results obtained for a fuel-burn optimized geared intercooled pulsed detonation (IC-PDC) turbofan are presented and discussed. For comparison, results obtained for the reference turbofan (ref. 2050) and for a geared non-intercooled pulsed detonation core (PDC-1) are also given. To quantify the impact of neglecting the auto-ignition delay time constraint, a second test case containing a non-intercooled pulsed detonation core (PDC-2) without HPC T/O temperature (T_3) limitation is also introduced. The effect of intercooler variability across the different mission phases on engine performance is afterwards quantified. This is achieved by controlling the amount of intercooler cooling flow passing through the external side of the HEX. Finally, the associated EINO$_x$ are quantified for different fuel-air-ratio levels.

The performance data obtained for the four optimal engines are listed in Table 5. Data is given for T/O conditions unless 'cruise' or 'TOC' are specified. In Table 4 some key PDC performance data is also given to support the discussion. The most significant difference between the engines is the OPR. The intercooler allows for a significant increase in mechanical compression without violating the HPC outlet temperature constraint. The OPR of the non-intercooled pulsed detonation core (PDC-1) is significantly lower due to a more stringent temperature limitation at T/O which limits the compression system pressure ratio (π_{comp}) provided by the compressors and fan.

The OPR of the non-intercooled pulsed detonation core, without T/O temperature constraint, and reference engine are similar across the different mission points. However, the compression system pressure ratio, π_{comp}, in the pulsed detonation core is 20% lower. The higher specific core power provided by the non-intercooled and intercooled pulsed detonation cores also allows for an increase in BPR and decrease in fan pressure ratio, and contributes slightly to an increase in propulsive efficiency at cruise.

The optimal pressure split exponential ratio n is equal to 0.4 in line with the findings of [13]. It is noted that this parameter is not affected by the presence of the PDC since the location of the intercooler is dependent on installation losses and on a particular intercooler design and concept.

Regarding weight, the intercooled pulsed detonation core is the heaviest engine. It is noted that the pulsed detonation combustor weight increases in the intercooled core relative to the non-intercooled configuration, despite a reduction in the number of tubes. Such increase in weight is primarily driven by the significantly larger design pressures in the intercooled PDC engine.

Regarding CO_2 emissions, these are directly proportional to fuel burn. The intercooled pulsed detonation turbofan, despite its weight and size, is the most fuel-efficient engine, providing a fuel burn reduction of around 10%. The non-precooled pulsed detonation core (PDC-1) accounts for a 6.2% reduction in fuel burn. If the auto-ignition delay constraint is neglected (PDC-2) the optimized non-intercooled PDC performance is allowed to increase and deliver a 7.2% improvement in fuel burn. The acquired results, clearly show that there is a synergy between intercooling and PDC allowing to achieve higher OPR while obeying the cycle temperature limits.

4.1 Cycle variability

The effect of cycle variability can be estimated by controlling the amount of intercooler heat rejection at different mission phases. Variability is achieved through the usage of a variable area nozzle, which controls the amount of cooling flow passing through the intercooler outer side. Opening the variable area nozzle maximizes intercooler efficiency and increases intercooler external side pressure

TABLE 4. Key PDC performance and design data.

Parameter	PDC-1	PDC-2	IC-PDC
ϕ	0.7	0.7	0.7
T_b K	2501	2569	2496
P_b (bar)	80	106	167
M_{CJ}	3.04	2.91	3.08
π_{PDC}	1.47	1.37	1.50
π_{PDC} (TOC)	1.50	1.38	1.53
π_{PDC} (cruise)	1.46	1.35	1.46
PDC mass (kg)	280	364	444
PDC nr. of tubes	24	20	10

losses. The intercooler cooling mass flow is typically increased at T/O to limit the cycle temperatures and reduced at TOC and cruise to minimize core heat rejection and pressure losses. For the present analysis, the variable area nozzle is fully opened at T/O to maximize intercooling, but it is allowed to vary at TOC and cruise.

Fig. 11 shows the variation of SFC reduction, relative to the ref. 2050 turbofan, with the variable area nozzle percentage (%) of opening at TOC and cruise. Previous results reported in [13] for a geared intercooled turbofan, revealed that the optimum nozzle opening is around 60% for TOC and 30% at cruise. The present data suggest that the variable area nozzle should be allowed to increase its area for both operating conditions (red square in Fig. 11) and slightly decrease the cycle average temperature at TOC and cruise. There is indeed a benefit in a limited decrease in HPC delivery temperature, at cruise and TOC, since it allows the PDC system to deliver higher

TABLE 5. Performance data for optimized reference 2050 and optimized intercooled PDC engines.

Parameter	2050 ref.	PDC-1	PDC-2	IC-PDC
OPR	59.0	45.7	61.03	99.2
OPR (TOC)	77.0	59.05	78.18	133.1
OPR (cruise)	61.5	48.32	64.09	106.2
π_{FAN} (outer)	1.39	1.38	1.37	1.31
π_{IPC}	2.30	2.79	2.80	4.46
π_{HPC}	20.2	8.89	12.70	12.34
π_{comp}	59.0	31.3	44.5	66.0
n	NA	NA	NA	0.4
BPR	16.2	20.76	19.6	26.76
Core mass flow (kg/s)	58.83	47.64	50.95	42.68
T_3 (K)	1053	880	973	858
T_3 (TOC) (K)	1012	839	932	818
T_3 (cruise) (K)	860	718	797	737
T_4 (K)	1920	1921	1920	1916
η_{prop} (cruise)	0.831	0.830	0.835	0.841
$\eta_{thermal}$ (cruise)	0.52	0.546	0.549	0.564
SFC (cruise) (mg/N.s)	12.65	12.05	11.93	11.54
IC mass (kg)	NA	NA	NA	332
Fan Diameter (m)	2.85	2.87	2.90	3.07
Engine mass (kg)	5078	4994	5236	5805
Engine architecture	1-3-10-2-4	1-4-6-1-5	1-4-8-2-5	1-6-7-2-6
ΔFB	datum	-6.2%	-7.2%	-10.0%

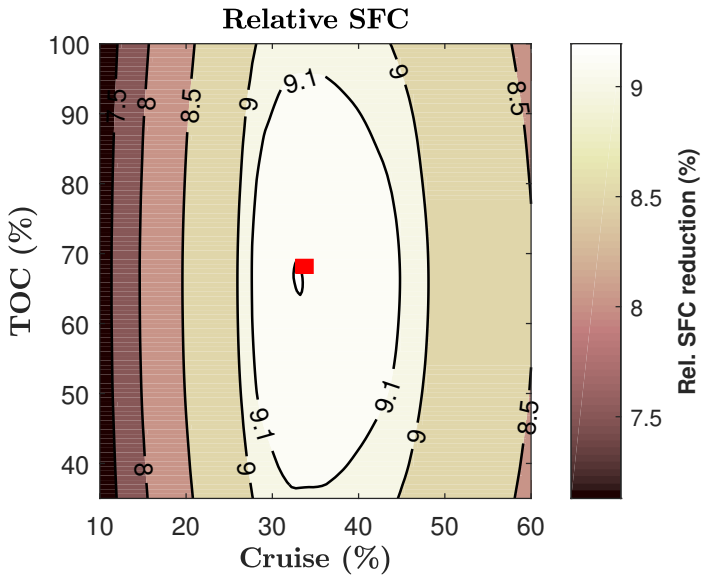

FIGURE 11. Relative SFC reduction with percentage of variable area nozzle at TOC and cruise. ■ – Optimal combination of N2 opening.

combustion pressure ratios.

4.2 $EINO_x$ estimation

In this section, the levels of NO_x associated with the three engines featuring a pulsed detonation combustor are quantified using the $EINO_x$ model proposed in this paper. The results are obtained for different levels of equivalence ratios in order to quantify the benefit arising from detonating in fuel-lean mixtures. Fuel-rich mixtures are not quantified in the present analysis due to the further need of including a secondary combustor to burn the excess fuel. Moreover, fuel-lean mixtures favor engine performance and allow to indirectly reduce NO_x by burning less fuel.

Figure 12 shows the results obtained when the PDC is allowed to operate with a stoichiometric mixture (ϕ = 1). The red circles represent the $EINO_x$ generated by the intercooled PDC engine and the blue squares represent the $EINO_x$ generated by the non-intercooled PDC engine (PDC-1). Both engines produce a significant amount of $EINO_x$. For comparison, the Trent 772, which serves as year 2000 reference for NO_x emissions, accounts for 35.56 g/kg fuel at T/O conditions [36]. If a slightly leaner mixture is selected (ϕ = 0.7, Fig 13-a) the $EINO_x$ generated by the geared intercooled PDC engine at T/O and TOC, decreases by about 5% and 24%, respectively (relative to the ϕ = 1 case). In the present study the only solution utilized to generate more acceptable levels of NO_x is to assume that the PDC is capable to detonate with extreme lean mixtures (ϕ = 0.6), see Fig. 13-b). The contour plot in Fig. 13-b) is limited to the CFD converged combination of pressures and temperatures for the ϕ = 0.6 test cases. Extrapolated $EINO_x$ data for the ϕ = 0.6 case is given in Table 6 to support the discussion but should be used with care. A 77% reduction in $EINO_x$, relative to the ϕ = 1 test case at T/O conditions, can be accomplished. However, it should again be noted that it is extremely hard to detonate in lean jet-A mixtures. This

was also the case in the present CFD computations, where several combinations of pressure and temperature did not allowed to achieve a sustained detonation wave.

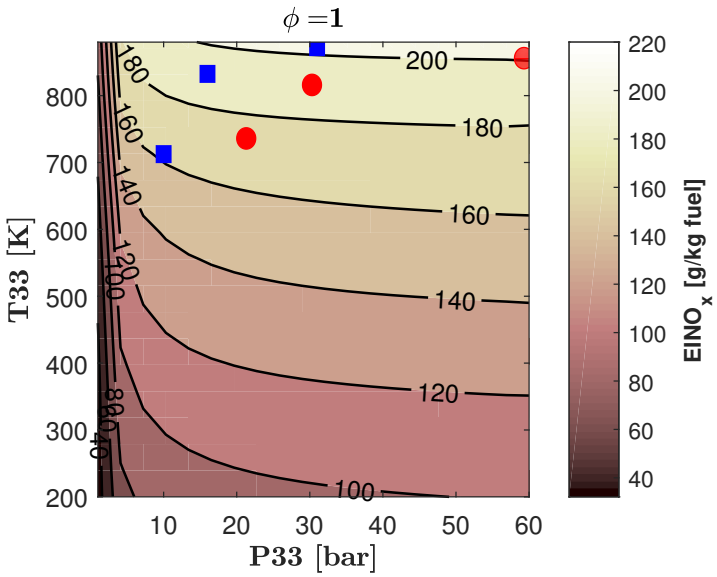

FIGURE 12. EINO$_x$ results obtained for ϕ = 1. ■ – PDC-1; ● – Intercooled PDC

The ICAO [37] parameter used for gaseous emissions consists of the NO$_x$ mass (g) emitted during the reference landing and take-off (LTO) cycle per kN of rated thrust at sea level,

$$\mathrm{EI} = \mathrm{EINO_x} \cdot \mathrm{SFC} \cdot t = \Psi \cdot t \tag{17}$$

Assuming a fixed time (t) in mode, a new metric, Ψ (g/kN-hr), can be derived to characterize the engines concerning NO$_x$ emissions. In practice, a comparison between the engines using this metric is more suitable since it also accounts for the effects of engine performance. The intercooled and non-intercooled PDC engines are compared in Table 6. The NO$_x$ results obtained with the two different cases without intercooling (PDC-1 and 2) are tabulated to quantify what is the effect of constraining the detonation inlet temperature at T/O in NO$_x$ emissions.

The usage of intercooling clearly results in better engine performance but with a penalty in NO$_x$ for the two fuel-lean mixtures (ϕ = 0.6 – 0.7), when compared with PDC-1. This is because, despite operating at similar inlet temperature, the PDC inlet pressure, P_{33}, doubles for the intercooled test case. This results in an increase of detonation plateau pressure from 80 bar to 167 bar, whereas the plateau temperature is kept constant around 2500 K. Figure 13 shows that for the fuel-lean test cases there is a slightly stronger

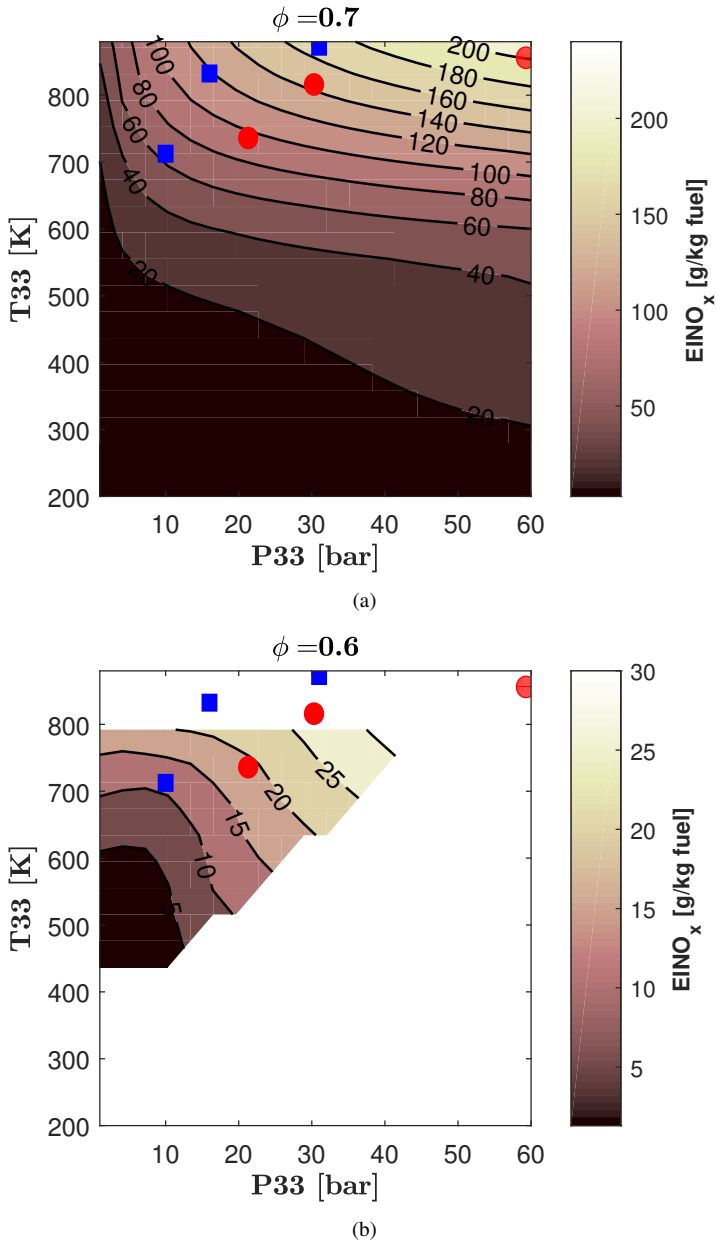

FIGURE 13. EINO$_x$ results obtained for: a) ϕ = 0.7; b) ϕ = 0.6. ■ – PDC-1; ● – Intercooled PDC

dependency of EINO$_x$ on pressure, when compared to the stoichiometric test cases, where EINO$_x$ pressure dependency is stronger for lower inlet pressures.

The NO$_x$ emissions expected to be produced by the non-intercooled PDC (PDC-2) are the highest for all equivalence ratios. The aforementioned behavior was expected due to the higher cycle temperatures occurring in all mission points when no constraint is applied to the T/O HPC delivery temperature. It is noted that for PDC-2 the T/O and TOC EINO$_x$ values were extrapolated beyond the table

limit due to the high temperatures involved.

5 Conclusions

In the present work, the CO_2 and NO_x emissions of an optimized geared intercooled PDC turbofan engine were estimated. For comparison, a reference geared turbofan engine, featuring a conventional burner, and a geared turbofan featuring a PDC were also developed and optimized for fuel-burn.

A model that predicts $EINO_x$ for different combinations of equivalence ratio, inlet temperature, and inlet pressure was also developed to quantify the benefits of combining intercooling and PDC systems. This paper allowed for the first time to estimate the impact of PDC, operating with jet-A at different equivalence ratios, in NO_x formation using relevant pressures and temperatures expected to occur in state of the art 2050 gas turbine applications for long-range civil aircraft.

TABLE 6. $EINO_x$ Results computed for the PDC and intercooled PDC turbofan engines.

ϕ = 1.0, Ψ (g/kN-hr)			
	PDC-1	PDC-2	Intercooled PDC
T/O	5744	6428 (extrap.)	5127
TOC	9115	10070(extrap.)	8569
Cruise	7196	7916	7280
ϕ = 0.7, Ψ (g/kN-hr)			
	PDC-1	PDC-2	Intercooled PDC
T/O	4808	6025 (extrap.)	4942
TOC	5452	7401 (extrap.)	6505
Cruise	2970	4508	4064
ϕ = 0.6, $EINO_x$ (g/kg fuel)			
	PDC-1	PDC-2	Intercooled PDC
T/O	33.7 (extrap.)	44.1 (extrap.)	43.5 (extrap.)
TOC	25.1 (extrap.)	34.4 (extrap.)	28.2 (extrap.)
Cruise	11.9	21.2	18.3
ϕ = 0.6, Ψ (g/kN-hr)			
	PDC-1	PDC-2	Intercooled PDC
T/O	941 (extrap.)	1208 (extrap.)	1102 (extrap.)
TOC	1183 (extrap.)	1600 (extrap.)	1264 (extrap.)
Cruise	516	908	760.43

The geared intercooled PDC engine was the most fuel-efficient solution. However, all PDC engine configurations produce prohibitive amounts of NO_x, even when compared with conventional year 2000 technology. Detonation in lean mixtures allowed for a significant reduction of NO_x emissions, but achieving detonation on the lean side of stoichiometric is very difficult if even possible to realize.

One solution to reduce NO_x formation could be the use of stratified charges, where a stoichiometric mixture is avoided by dividing the tube into rich and lean zones. Fuel-rich mixtures should be located near the closed end of the tube to promote a rapid initiation of detonation. The detonation wave then propagates into a fuel-lean mixture, which is located near the open end of the tube. However, homogeneous rich and lean zones should be tough to accomplish in practical applications. Results from [4] showed that the usage of stratified charge could result in a 70% reduction of NO_x formation in jet-A.

Another solution could be the injection of steam or re-circulation of cold exhaust gases. Both techniques were explored in [6] with relative success. However, changing the properties of the flow at the inlet will, in turn, affect the detonability of the mixture and these techniques should, therefore, be employed with care. Moreover, in aero-engines weight is a significant constraint, and a lightweight system should be preferred.

ACKNOWLEDGMENT

The E.U. financially supports this work under the "ULTIMATE – Ultra Low Emission Technology Innovations for Mid-century Aircraft Turbine Engines" Project co-funded by the European Commission within the Horizon 2020 Programme (2014-2020) under Grant Agreement no. 633436. The CFD computations were performed on resources at Chalmers Centre for Computational Science and Engineering (C3SE) provided by the Swedish National Infrastructure for Computing (SNIC).

REFERENCES

[1] Grönstedt, T., Xisto, C., Sethi, V., Rolt, A., Rosa, N. G., Seitz, A., Yakinthos, K., Donnerhack, S., Newton, P., Tantot, N., Schmitz, O., and Lundbladh, A., 2016. "Ultra low emission technology innovations for mid-century aircraft turbine engines". In ASME Turbo Expo: Turbomachinery Technical Conference and Exposition, Seoul, South Korea., no. GT2016-56123.

[2] Grönstedt, T., Irannezhad, M., Lei, X., Thulin, O., and Lundbladh, A., 2014. "First and second law analysis of future aircraft engines". *ASME J Eng Gas Turb Power,* **136**(3), pp. 031202–031202–10.

[3] Xisto, C., Ali, F., Petit, O., Grönstedt, T., Rolt, A., and Lundbladh, A., 2017. "Analytical model for the performance estimation of pre-cooled pulse detonation turbofan engines". In ASME Turbo Expo: Turbomachinery Technical Conference and Exposition, Charlotte, NC, USA, no. GT2017-63776.

[4] Yungster, S., and Breisacher, K., 2005. "Study of NOx formation in hydrocarbon-fueled pulse detonation engines". In 41st AIAA/ASME/SAE/ASEE Joint Propulsion Conference, Tucson, Arizona, no. AIAA 2005-4210.

[5] Yungster, S., Radhakrishnan, K., and Breisacher, K., 2006. "Computational study of NOx formation in hydrogen-fuelled pulse detonation engines". *Combustion Theory and Modelling,* **10**(6), pp. 981–1002.

[6] Djordjevic, N., Hanraths, N., Gray, J., Berndt, P., and Moeck, J., 2017. "Numerical study on the reduction of NOx emissions from pulse detonation combustion". In ASME Turbo Expo: Turbomachinery Technical Conference and Exposition, Charlotte, NC, USA, no. GT2017-64485.

[7] ANSYS, 2016. *ANSYS Fluent Theory Guide*. ANSYS Inc.

[8] Djordjevic, N., Hanraths, N., Gray, J., Berndt, P., and Moeck, J., 2017. "Numerical study on the reduction of NOx emissions from pulse detonation combustion". *ASME J Eng Gas Turb Power,* **140**(4), pp. 041504–041504–7.

[9] Grönstedt, T., 2000. "Development of methods for analysis and optimization of complex jet engine systems". Ph.d. thesis, Chalmers University of Technology, Gothenburg, Sweden.

[10] Grönstedt, T., and Wallin, M., 2004. "A comparative study of genetic algorithms and gradient methods for RM12 turbofan engine diagnostics and performance estimation, vienna, austria.". In ASME Turbo Expo: Turbomachinery Technical Conference and Exposition,, no. GT2004-53591.

[11] Xu, L., and Gronstedt, T., 2010. "Design and analysis of an intercooled turbofan engine". *ASME J Eng Gas Turb Power,* **132**(11), pp. 114503–1–4.

[12] Xu, L., Kyprianidis, K. G., and Gronstedti, T. U. J., 2013. "Optimization study of an intercooled recuperated aero-engine". *J. Propul. Power,* **29**(2), pp. 424–432.

[13] Zhao, X., Thulin, O., and Gronstedt, T., 2015. "First and second law analysis of intercooled turbofan engine". *ASME J Eng Gas Turb Power,* **138**(2), pp. 021202–021202–8.

[14] Thulin, O., Petit, O., Xisto, C., Zhao, X., and Gronstedt, T., 2017. "First and second law analysis of radical intercooling concepts". *ASME J Eng Gas Turb Power,* **140**(8), pp. 081201–0812011–10.

[15] Newton, P., Tantot, N., Donnerhack, S., and Lundbladh, A., 2015. D1.1 - Establish common year 2050 technology level assumptions. Report, H2020 - ULTIMATE project.

[16] Greitzer, E. M., Bonnefoy, P. A., delaRosaBlanco, E., Dorbian, C. S., Drela, M., Hall, D. K., Hansman, R. J., Hileman, J. I., Liebeck, R. H., and Lovegren, J., 2010. N+3 aircraft concept designs and trade studies. volume 2; appendices-design methodologies for aerodynamics, structures, weight, and thermodynamic cycles. Report CR-2010-216794/VOL2, E-17419-2, NASA.

[17] Zhao, X., and Gronstedt, T., 2015. "Conceptual design of a two-pass cross-flow aeroengine intercooler". *Proceedings of the Institution of Mechanical Engineers Part G-Journal of Aerospace Engineering,* **229**(11), pp. 2006–2023.

[18] Zhao, X., Tokarev, M., Hartono, E. A., Chernoray, V., and Grönstedt, T., 2016. "Experimental validation of the aerodynamic characteristics of an aero-engine intercooler". *ASME J Eng Gas Turb Power,* **139**(5), pp. 051201–051201–10.

[19] Kays, W. M., and L, L. A., 1964. *Compact Heat Exchangers*. McGraw-Hill, New York.

[20] Kyprianidis, K. G., Rolt, A. M., and Gronstedt, T., 2014. "Multidisciplinary analysis of a geared fan intercooled core aero-engine". *ASME J Eng Gas Turb Power,* **136**(1), pp. 011203–011203–11.

[21] Marek, C. J., Papathakos, L. C., and Verbulecz, P. W., 1977. Preliminary studies of autoignition and flashback in a premixing-prevaporizing flame tube using Jet-A fuel at lean equivalence ratios. Report TMX-3526, NASA.

[22] St. George, A., Driscoll, R., Gutmark, E., and D., M., 2014. "Experimental comparison of axial turbine performance under steady and pulsating flows". *J Turbomach,* **136**(11), pp. 111005–111005–11.

[23] Rouser, K. P., King, P. I., Schauer, F. R., Sondergaard, R., Hoke, J. L., and Goss, L. P., 2014. "Time-resolved flow properties in a turbine driven by pulsed detonations". *J. Propul. Power,* **30**(6), pp. 1528–1536.

[24] Rasheed, A., Furman, A. H., and Dean, A. J., 2009. "Pressure measurements and attenuation in a hybrid multitube pulse detonation turbine system". *J. Propul. Power,* **25**(1), pp. 148–161.

[25] St. George, A., 2016. "Development and testing of pulsed and rotating detonation combustors". Ph.d thesis, University of Cincinnati, Cincinnati, Ohio, USA.

[26] Suresh, A., Hofer, D. C., and Tangirala, V. E., 2012. "Turbine efficiency for unsteady, periodic flows". *ASME J Turbomach,* **134**(3), pp. 034501–034501–6.

[27] Rolt, A., Sethi, V., Jacob, F., Sebastiampillai, J., Xisto, C., Grönstedt, T., and Raffaelli, L., 2017. "Scale effects on conventional and intercooled turbofan engine performance". *The Aeronautical Journal,* **121**(1242), pp. 1162–1185.

[28] Pera, R. J., Onat, E., Klees, G., and Tjonneland, E., 1977. A method to estimate weight and dimensions of aircraft gas turbine engines. Report CR-159481, NASA.

[29] Korsia, J.-J., and Spiegeleer., G. D., 2006. "VITAL, an European R&D program for greener aero-engines". In 25th Congress of International Council of the Aeronautical Sciences, Hamburg, Germany.

[30] Wilfert, G., Sieber, J., Andrew Rolt, N. B., Touyeras, A., and Colantuoni, S., 2007. "New environmental friendly aero engine core concepts". In XVIII International Symposium of Air Breathing Engines, Beijing, China, no. ISABE-2007-1120.

[31] Larsson, L., Grönstedt, T., and Kyprianidis, K. G., 2011. "Conceptual design and mission analysis for a geared turbofan and an open rotor configuration". In ASME Turbo Expo: Turbomachinery Technical Conference and Exposition, no. GT2011-46451.

[32] Kyprianidis, K., Dax, A., Ogaji, S., and Grönstedt, T., 2009. "Low pressure system component advancements and its impact on future turbofan engine emissions". In XIX International Symposium on Air Breathing Engines, Montreal, Canada., no. ISABE-2009-1276.

[33] Zhao, X., 2016. "Aero engine intercooling". Ph.d. thesis, Chalmers University of Technology, Gothenburg, Sweden.

[34] Heinemann, P., Panagiotou, P., Vratny, P., Kaiser, S., Hornung, M., and Yakinthos, K., 2017. "Advanced tube and wing aircraft for year 2050 timeframe". In 55th AIAA Aerospace Sciences Meeting, Grapevine, Texas., no. AIAA 2017-1390.

[35] Gill, P. E., Murray, W., Saunders, M. A., and Wright, M. H., 1983. "Computing forward-difference intervals for numerical

optimization". *Siam Journal on Scientific and Statistical Computing,* **4**(2), pp. 310–321.

[36] EASA, 2018. ICAO aircraft engine emissions databank nr. 9. https://www.easa.europa.eu/easa-and-you/environment/icao-aircraft-engine-emissions-databank., Accessed on June, 26.

[37] ICAO, 2008. *Enviromental Protection, Annex 16 Vol. 2*. ICAO, Montréal, Quebec, Canada.

List of Figures

List of Tables

APPENDIX

TABLE 7. REACTION MECHANISM FOR JET-A–AIR DETONATION[a]

No.	Reaction	A	B	E
	Two-stage fuel pyrolisis			
1	$C_{12}H_{23} + O_2 \longrightarrow 5\,C_2H_4 + C_2H_3 + O_2$	3.00E+07	1.5	65.7
2	$C_{12}H_{23} + OH \longrightarrow 6\,C_2H_4 + O$	2.00E+10	1.0	37.4
	Hydrogen-oxygen chain			
3	$H + O_2 \longrightarrow OH + O$	3.52E+16	-0.7	71.4
4	$OH + O \longrightarrow H + O_2$	1.15E+14	-0.3	-0.7
5	$OH + H_2 \longrightarrow H_2O + H$	1.17E+09	1.3	15.2
6	$H_2O + H \longrightarrow OH + H_2$	6.72E+09	1.3	84.6
7	$O + H_2O \longrightarrow 2\,OH$	7.60E+00	3.8	53.5
8	$2\,OH \longrightarrow O + H_2O$	2.45E-01	4.0	-19.0
	Hydroperoxyl formation and consumption			
9[b]	$H + O_2 + M \longrightarrow HO_2 + M$	6.76E+19	-1.4	0.0
10	$HO_2 + H \longrightarrow 2\,OH$	1.70E+14	0.0	3.7
11	$HO_2 + H \longrightarrow H_2 + O_2$	4.28E+13	0.0	5.9
12	$HO_2 + OH \longrightarrow H_2O + O_2$	2.89E+13	0.0	-2.1
	Hydrogen peroxide formation and consumption			
13	$2\,HO_2 \longrightarrow H_2O_2 + O_2$	3.02E+12	0.0	5.8
14[c]	$H_2O_2 + M \longrightarrow 2\,OH + M$	1.20E+17	0.0	190.0
	Direct recombination			
15[b]	$H + OH + M \longrightarrow H_2O + M$	2.20E+22	-2.0	0.0
16[b]	$H_2O + M \longrightarrow H + OH + M$	2.18E+23	-1.9	499.0
	Carbon monoxide reactions			
17	$CO + OH \longrightarrow CO_2 + H$	4.40E+06	1.5	-3.1
18	$CO_2 + H \longrightarrow CO + OH$	4.97E+08	1.5	89.7
	Initiation and fuel consumption			
19	$C_2H_4 + O_2 \longrightarrow C_2H_3 + HO_2$	4.22E+13	0.0	241.0
20	$C_2H_4 + OH \longrightarrow C_2H_3 + H_2O$	2.70E+05	2.3	12.4
21	$C_2H_4 + O \longrightarrow CH_3 + CHO$	2.25E+06	2.1	0.0
22	$C_2H_4 + O \longrightarrow CH_2CHO + H$	1.21E+06	2.1	0.0
23	$C_2H_4 + HO_2 \longrightarrow C_2H_3 + H_2O_2$	2.23E+12	0.0	71.9
24	$C_2H_4 + H \longrightarrow C_2H_3 + H_2$	2.25E+07	2.1	55.9
25	$C_2H_4 + H \longrightarrow C_2H_5$			
	k_∞	1.52E+13	0.03	13.0
	k_0	1.17E+16	0.03	-28.0
	Vinyl, methyl and ethyl consumption			
26	$C_2H_3 + H \longrightarrow C_2H_2 + H_2$	3.00E+13	0.0	0.0
27	$C_2H_3 + O_2 \longrightarrow CH_2O + CHO$	1.70E+29	-5.3	27.2
28	$C_2H_3 + O_2 \longrightarrow CH_2CHO + O$	7.00E+14	-0.6	22.0
29	$CH_3 + O_2 \longrightarrow CH_2O + OH$	3.30E+11	0.0	37.4
30	$CH_3 + O \longrightarrow CH_2O + H$	8.43E+13	0.0	0.0
31	$C_2H_5 + O_2 \longrightarrow C_2H_4 + HO_2$	2.00E+12	0.0	20.9
32	$C_2H_5 \longrightarrow C_2H_4 + H$			
	k_∞	1.30E+13	0.0	167.0
	k_0	1.00E+16	0.03	126.0
	Vinoxy, ketene, formaldehyde, formyl and acetylene consumption			
33	$CH_2CHO \longrightarrow CH_2CO + H$	1.05E+37	-7.2	186.0
34	$CH_2CO + H \longrightarrow CH_3 + CO$	1.11E+07	2.0	8.4
35	$CH_2O + OH \longrightarrow CHO + H_2O$	3.90E+10	0.9	1.7
36[d]	$CHO + M \longrightarrow CO + H + M$	1.86E+17	-1.0	71.1
37	$CHO + O_2 \longrightarrow CO + HO_2$	3.00E+12	0.0	0.0
38	$C_2H_2 + OH \longrightarrow CH_2CO + H$	1.90E+07	1.7	4.2
	Extended Zeldovich mechanism			
39	$N + N + M \longleftrightarrow N_2 + M$	2.80E+17	-0.8	0.0
40	$N + O_2 \longleftrightarrow NO^+O$	6.40E+09	1.0	26.4
41	$N + NO \longleftrightarrow N_2 + O$	1.60E+13	0.0	0.0
42	$N + OH \longleftrightarrow NO + H$	6.30E+11	0.5	0.0
43	$HO_2 + NO \longleftrightarrow NO_2 + OH$	3.40E+12	0.0	-1.1
44	$H + NO_2 \longleftrightarrow NO + OH$	3.50E+14	0.0	6.3
45	$O + NO_2 \longleftrightarrow NO + O_2$	1.00E+13	0.0	2.5
46	$NO_2 + M \longleftrightarrow NO + O + M$	1.16E+16	0.0	276.3

[a]Forward rate coefficient $k = AT^B exp(-E/RT)$, A units mole-cm-s-K, E units KJ/mole

[b]Third-body efficiencies: CO = 1.9; CO_2 = 3.8; H_2 = 2.5; H_2O = 12.0

[c]Third-body efficiencies: same as b except H_2O = 16.3

[d]Third-body efficiencies: CO = 2.5; CO_2 = 2.5; H_2 = 1.9; H_2O = 12.0

